applied sciences

MDPI

Article

Experimental Analysis and Optimisation of a Novel Laser-Sintering Process for Additive Manufacturing of Continuous Carbon Fibre-Reinforced Polymer Parts

Michael Baranowski [1,2,*], Lukas Völger [1], Marco Friedmann [1] and Jürgen Fleischer [1]

[1] Institute of Production Science, Faculty of Mechanical Engineering, Karlsruhe Institute of Technology (KIT), Kaiserstaße 12, 76131 Karlsruhe, Germany
[2] Karlsruhe Research Factory, Karlsruhe Institute of Technology (KIT), Rintheimer Querallee 2, 76131 Karlsruhe, Germany
* Correspondence: michael.baranowski@kit.edu; Tel.: +49-1523-9502642

Abstract: Additive manufacturing of continuous carbon fibre-reinforced polymer (CCFRP) parts enables the production of high-strength parts for aerospace, engineering and other industries. Continuous fibres allow for parts to be reinforced along the load path, multiplying their mechanical properties. However, current additive manufacturing processes for producing CCFRP parts do not optimally meet the requirements of the matrix. With resin- and extrusion-based processes, the time-consuming and costly post-processing required to remove support structures severely limits design freedom, and producing small batches requires increased effort. In contrast, laser sintering has proven to be a promising alternative in an industrial environment, allowing the production of robust parts without support structures in a time-efficient and economical manner for single and small-batch production. Based on a novel laser-sintering machine with the automated integration of continuous fibres, a combination of the advantages of the laser-sintering process and the advantages of continuous fibres is to be achieved. This paper describes an experimental analysis and optimisation of this laser-sintering machine using design of experiments. The processing time for fibre integration could be reduced by a factor of three compared to the initial state.

Keywords: laser sintering (LS); continuous carbon fibre-reinforced polymer parts (CCFRPs); fibre integration unit; heat affected zone; split-plot design (SPD); central composite design (CCD)

Citation: Baranowski, M.; Völger, L.; Friedmann, M.; Fleischer, J. Experimental Analysis and Optimisation of a Novel Laser-Sintering Process for Additive Manufacturing of Continuous Carbon Fibre-Reinforced Polymer Parts. *Appl. Sci.* **2023**, *13*, 5351. https://doi.org/10.3390/app13095351

Academic Editor: Guijun Bi

Received: 30 March 2023
Revised: 17 April 2023
Accepted: 23 April 2023
Published: 25 April 2023

1. Introduction

The use of continuous carbon fibre-reinforced polymer (CCFRP) parts in industrial applications offers enormous potential to significantly reduce future products' consumption and CO_2 emissions economically and effectively [1]. CCFRP parts are characterised by their low weight-to-strength ratio and high mechanical tensile properties along the fibre direction. By using continuous fibres, the mechanical properties of fibre-reinforced parts can be increased along the load path [2].

Additive manufacturing processes offer a promising approach for the tool-less and time-efficient production of CCFRP parts with a high degree of individualisation and shape complexity. Material extrusion (MEX), such as fused layer modelling (FLM) or ARBURG plastic free-forming (APF), is well established in the literature for the additive manufacturing of CCFRP parts [3–10]. Another category of processes for CCFRP parts is vat photopolymerisation (VPP) [11–13]. CCFRP parts produced by these processes (MEX and VPP), however, do not optimally meet the quality requirements for the matrix. Due to the nature of these processes, support structures are required, which have to be removed and disposed of after production. This results in the time- and cost-effective disposal and post-processing steps. In addition, the use of support structures limits the ability to create overhangs, cavities and undercuts, which results in limited part complexity. Furthermore,

the breaking off of support structures can cause surface defects on the remaining part surfaces and, thus, lead to a more inhomogeneous appearance of the parts. Moreover, MEX and VPP do not allow for economic small-batch production.

By contrast, the laser-sintering (LS) process represents a promising alternative for producing CCFRP parts. In a process comparison among MEX, VPP and LS with regard to the mechanical and thermal properties, as well as the long-term stability of the polymer parts produced, the LS process proves to be particularly advantageous, since the LS process enables the production of robust functional parts in injection moulding quality [14,15]. According to [14], the Young's modulus of laser-sintered specimens is higher than the values determined for the Young's modulus of injection-moulded specimens, which is caused by a higher degree of crystallinity of the molecular structure of the semi-crystalline thermoplastics. The tensile strength was almost identical to that of the injection-moulded specimens. Other advantages of the LS process are the absence of support structures and the associated greater design freedom. In the LS process, the unsintered powder acts as a support structure, eliminating the need for time-consuming and costly post-processing steps [16]. By realising undercuts, cavities and overhangs, LS can produce near net-shape functional parts with high complexity in a single process step. Due to the ability to compactly position parts vertically and horizontally in the powder bed, the LS process allows for the economical production of small batches [14,17]. Compared to FLM parts, LS parts have up to three times less anisotropy, higher dimensional accuracy and less surface roughness [14,17,18]. The LS process, thus, produces polymer parts with promising basic properties (matrix) for CCFRP parts. However, no commercially available LS machines combine the advantages of the LS process with the advantages of continuous fibres. Challenges to integrating continuous fibres in the LS process arise, particularly in the complex temperature control and the repetitive application movement of the recoater for each layer.

To combine the process-specific advantages of the LS process as well as the promising part properties with the advantages of continuous carbon fibres, the technical feasibility (i.e., the layered integration of continuous fibre rovings into laser-sintered parts made of PA12) was demonstrated in [19,20]. The core element of this prototypical LS machine is a fibre integration unit for integrating the rovings into the already manufactured layers of the part. A heated fibre nozzle is used to liquefy the polymer locally, creating a heat affected zone (HAZ) with a characteristic width and depth. The roving is then placed into the liquefied melt by a synchronised sequence of motions between the roving feed rate and the nozzle feed rate. In [20], the extended LS process was analysed regarding temperature management during fibre integration to identify operating points for curl-free integration of rovings. In [19], the influence of the process and material parameters on the shape of the HAZ was investigated using a simplified experimental setup. The results in [19,20] provide the first starting points for successful fibre integration and form the basis of this paper. However, the identified starting points lead to the inefficient production of CCFRP parts. The production speed is relatively slow, so the rovings can only be embedded into the part at a low feed rate. The low feed rate leads to an uneconomical and time-consuming production of CCFRP parts. In addition, the HAZ's width and depth are too large, so the rovings have to be placed far away from the part edges. The consequence of a too large HAZ is that the FVC and the associated mechanical properties can only be set low. Thus, the potential of this new LS process with continuous fibre integration remains undiscovered. A comprehensive understanding of the rovings' integration process in the developed LS machine is indispensable to achieve an economical production of LS parts with a high FVC and, thus, high mechanical properties. Only with knowledge of the main influencing variables and their interactions on the roving integration process is it possible to optimise the width and depth of the HAZ and the processing time in a targeted manner.

Therefore, this paper aimed to experimentally characterise and optimise this novel laser-sintering process with automated continuous fibre integration. Based on the identified and initial operating points in [19–21], the main influencing variables and interactions on

the formation process of the HAZ were systematically investigated using a split-plot design (SPD). In a subsequent study, the target variables were analysed more thoroughly using a central composite design (CCD). Section 2.1 first presents the principle of automated continuous fibre integration. The influencing variables on the fibre integration caused by the fibre integration unit, and the target variables to be optimised are discussed in the same section. The SPD is presented in Section 2.2. For a detailed analysis of the target variables at a predicted operating point, the procedure for the CCD is described in Section 2.3. Section 3 presents the results and their interpretation. Section 4 discusses the results in relation to the initial state.

In this study, an increase in the process time of 233% was demonstrated for the integration of the rovings. Thus, a more economical production of CCFRP parts in the developed LS machines is now possible. The width and depth of the HAZ were reduced by 56% and 44%, respectively, so the rovings can now be integrated closer to the part edges, and thus the fibre volume content (FVC) can be set higher. This study, therefore, provides optimised operating points for future research to increase the FVC and the associated mechanical properties systematically.

2. Materials and Methods

This section describes the principle of continuous fibre integration in the developed laser-sintering machine with respect to the influencing and target variables on the roving integration caused by the fibre integration unit. This paper does not provide a detailed description of the machine and the achievable part properties. This can be found in [19,20].

2.1. Principle of Continuous Fibre Integration

A description of the process flow is provided in this section to provide a basic understanding of roving integration in the LS machine developed. The starting point for roving integration is a heated process chamber of the LS machine of approximately 110 °C. After fresh powder has been applied by the recoater and the surface temperature of the powder bed has been homogenised by the IR emitters, the applied powder layer is melted by the laser beam. According to an ISO 6983 G-code, the layer-related (2D) integration of one or more rovings takes place sequentially. For this, the entire structure of the fibre integration unit is moved in rapid traverse in the x- and y-directions to the starting point of the first fibre path on the build platform. The fibre integration unit and its components are shown in Figure 1. A metal plate (additional heat source) heated to the temperature T_{HM3} and arranged parallel to the powder surface at the distance h_{HM3} on the bottom side of the fibre integration unit is used to keep the powder bed surface warm. This heating prevents premature crystallisation and the associated curling of the part. Heat transfer between a heated fibre nozzle at temperature T_D and the powder bed surface creates a local melt zone or heat affected zone (HAZ) with a shape describing the width b_{HAZ} and depth t_{HAZ} in the already melted layers of the part. At this point, the viscosity level of the polymer is locally reduced, and the polymer increasingly liquefies. Simultaneously with the melting process, the roving is bent between the face of the ring-shaped fibre nozzle and the generated HAZ by a drive and pressure roller, synchronised with the feed rate v_D of the nozzle. Due to the fact of its intrinsic heat and stiffness (influenced by a coating), the roving is immersed in the liquefied polymer and, thus, in the HAZ. The resulting melt wets the roving and fixes it to the underlying layers. A cutting blade cuts the roving to a length programmed in the G-code. The built-in diode laser (450 nm, 1.6 W) is inactive during the roving integration. Once the roving has been successfully integrated, the recoater applies fresh powder, and the laser melts the new layer of powder, fully embedding the roving in the polymer matrix. This process is repeated until all rovings are integrated according to the G-code. This is followed by the controlled cooling of the powder cake and the LS machine.

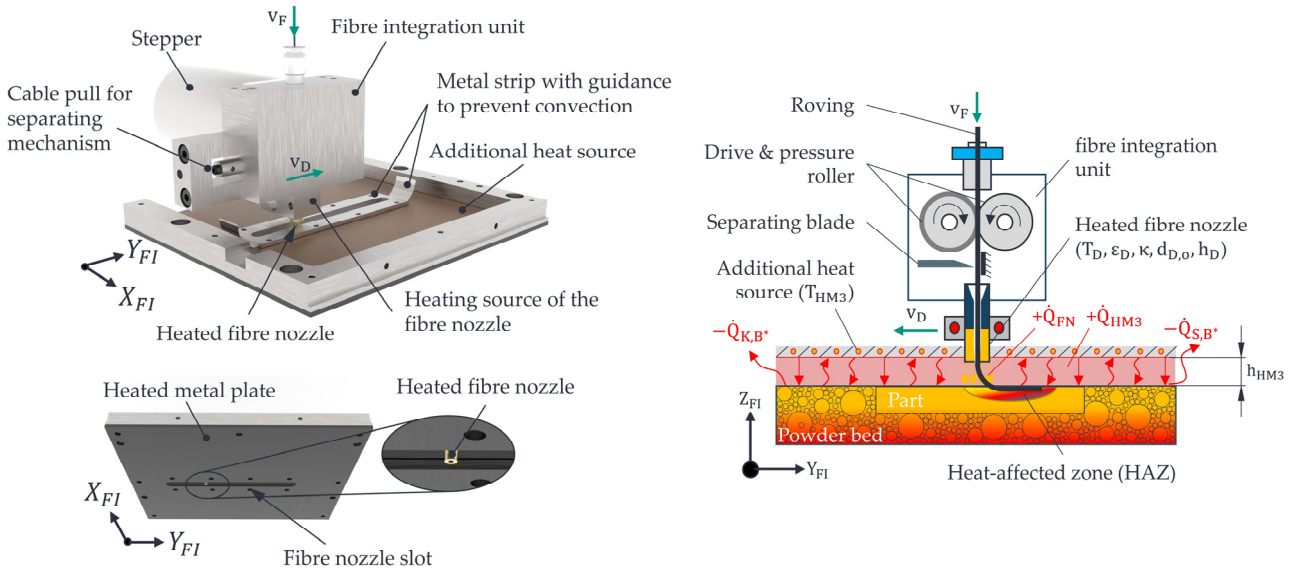

Figure 1. 3D view of the fibre integration unit (without powder bed) (**a**) and a schematic of the process zone (**b**) [22].

2.1.1. Influencing Factors on Roving Integration

An analytical consideration of the existing heat flows is used to derive the influencing variables. For simplicity, only one-dimensional heat flows were considered in this paper. The heat transferred during the roving integration can be described by the heat flows involved, as defined in Equation (1).

$$\dot{Q}_{FI} = \dot{Q}_{HM3} + \dot{Q}_{FN} \quad (1)$$

The additional and parallel heat source at the bottom of the fibre integration unit forms the first heat flow summand $\dot{Q}_{HM3}$. This constellation is a special case of free convection with internal flow within two parallel horizontal plates [23,24]. The additional heat source forms the hotter upper plate, and the powder bed surface forms the colder lower plate. According to [23], no flow is generated since the air is stably layered between the upper plate (heat source) and the lower plate (powder bed surface). As described in [23,24], heat is transferred mainly by conduction and radiation. The heat flow transferred to the powder bed surface by the additional heat source is given by Equation (2) below. All quantities are shown in Table 1.

$$\dot{Q}_{HM3} = \lambda_L \cdot A_{HM3} \cdot \frac{T_{HM3} - T_O}{h_{HM3}} + \frac{\sigma}{\frac{1}{\varepsilon_{HM3}} + \frac{1}{\varepsilon_P} - 1} \cdot A_{HM3} \cdot (T_{HM3}^4 - T_O^4) \quad (2)$$

The first summand in Equation (2) represents the heat conduction law applied to the LS machine. The second summand represents the Stefan–Boltzmann law with an additional radiation exchange between the additional heat source and the powder bed surface.

The second summand in Equation (1) represents the heat flow generated by the heated fibre nozzle. This heat flow is mainly responsible for the targeted transfer of heat energy and, thus, for HAZ formation. The heat flux transferred through the fibre nozzle is defined in Equation (3).

$$\dot{Q}_{FN} = \lambda_L \cdot A_D \cdot \frac{T_D - T_O}{h_D} + \frac{\sigma}{\frac{1}{\varepsilon_D} + \frac{1}{\varepsilon_P} - 1} \cdot \pi \cdot \left(r_{D,o}^2 - r_{D,i}^2\right) \cdot (T_D^4 - T_O^4) \quad (3)$$

Table 1. Influencing variables due to the integration concept with the setting range.

Symbol	Description	Unit	Setting	Setting Range
h_D	Distance between fibre nozzle and powder bed surface	mm	PLC	0–2
v_D	Feed rate of the fibre nozzle	mm/min	PLC	0–1000
v_R	Feed rate of the roving = feed rate of fibre nozzle	mm/min	PLC	0–1000
$d_{D,o} \mid d_{D,i}$	Outer $d_{D,o}$ and inner diameter $d_{D,i}$ of the fibre nozzle	mm	Lathe	$d_{D,o} \geq 2$ $d_{D,i} \geq 0.6$
A_{HM3}	Area of the heat source (metal sheet)	mm^2	Laser cutting	≈22,500
h_{HM3}	Distance of heat source (metal sheet) to powder surface = air gap width	mm	Feeler gauge tape	0–2
κ	Curvature of fibre nozzle	-	Lathe	Planar/concave
ε_D	Emissivity of fibre nozzle (black oxidised)	-	Varnish	0–1
ε_P	Emissivity of the powder (Sintratec PA12)	-	State of delivery	≈0.9
ε_{HM3}	Emissivity of the matt black painted metal sheet	-	Varnish	0–1
T_D	Fibre nozzle temperature	°C	PLC	. . . 400
T_O	Powder bed surface temperature	°C	PLC	. . . 200
T_{HM3}	Heat source temperature (metal sheet)	°C	PLC	. . . 200

The first summand in Equation (3) represents the heat conduction law between the ring-shaped fibre nozzle with inner diameter $d_{D,i}$ (guidance and transmission for the roving inside the fibre nozzle), outer diameter $d_{D,o}$, nozzle curvature κ and the powder bed surface. The second summand represents the Stefan–Boltzmann law with an additional radiation exchange between the front surface of the fibre nozzle and the powder bed surface. In $\dot{Q}_{FN}$, the time period t_{FN} of the heat transfer (i.e., the amount of heat energy transferred in a given time period) is also implied. The time period of the heat transfer can be influenced by the feed rate v_D of the fibre nozzle. Possible convection flows between the fibre nozzle and the additional heat source, as well as heat losses at the edges of the additional heat source to the surroundings, such as losses due to the fact of convection $\dot{Q}_{K,B}$ and radiation $\dot{Q}_{S,B}$, were assumed but not considered in this analysis.

The variables listed in Equations (2) and (3) summarise the influencing variables on the roving integration process in the developed laser-sintering machine and are listed in Table 1. This analysis did not consider influences due to the LS process ("laser–part interactions", material composition and ageing effects of the powder). They were kept constant as far as possible in the studies—see Sections 2.2 and 2.3.

Initial studies were carried out in [19,20] for the influencing variables listed in Table 1. Initial operating points were identified at which 1K rovings can be integrated into the part. These operating points form the starting point for the study with SPD described in Section 2.2. In addition, parallel to the execution of the SPD study and based on Equations (2) and (3), an FE model was developed in COMSOL Multiphysics to describe the formation process of the HAZ (without considering the roving). This FE model was validated with the results of the SPD in Section 2.2 and used to predict and constrain the possible solution space for the target variables to be optimised—see Section 2.3. The FE model is derived and described in more detail in [21].

2.1.2. Target Variables

The target variables for successfully integrating rovings within the developed LS machine are illustrated in Figure 2.

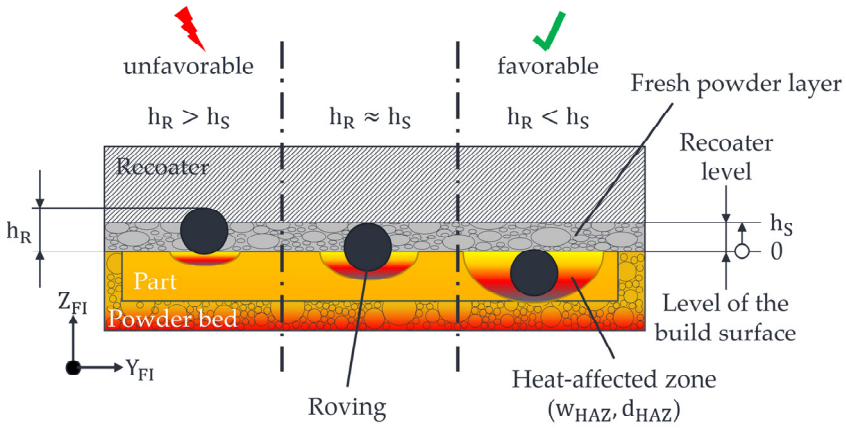

Figure 2. Schematic representation of the influence of the HAZ on the roving overlap h_R.

For successful roving integration, the HAZ must be created so that the roving is below the level of movement of the recoater at h_S (=set layer thickness in the printing process). In other words, the depth of the HAZ t_{HAZ} must be set so that the roving sinks deep enough into the melt, i.e., with $h_R < h_S$, and thus does not create a disturbing contour for the recoater (process reliability). The result of the FE model is, therefore, a value for t_{HAZ} corresponding to a roving thickness of 0.4 mm. If the roving extends too far out of the part ($h_R \geq h_S$), a collision between the recoater and the roving can occur during the subsequent recoating process. This will cause the part to be dragged by the recoater, and the printing process will have to be stopped. In addition, the width of the HAZ b_{HAZ} must be set as narrow as possible to place rovings as close to the edges of the part as possible without melting unsintered and loose powder outside the part edges. In addition, the HAZ's width and depth are expected to influence the achievable FVC in part strongly and, thus, on the attainable mechanical properties. To maximise the FVC in future considerations, the smallest possible values for b_{HAZ} and t_{HAZ} are targeted. For economical production, the processing time of the roving integration is also highly relevant. The processing time is given by the feed rate v_D of the fibre nozzle. The target values for successful fibre integration are summarised in Table 2.

Table 2. Summary of the target variables for a successful integration of rovings.

Symbol	Description	Unit
b_{HAZ}	Width of the heat affected zone	mm
t_{HAZ}	Depth of the heat affected zone	mm
v_D	Process time expressed by the nozzle feed rate	mm/min
h_R	Overlap of the roving as a measure of process reliability	mm

2.2. Study 1: Identification of Main Influencing Variables and Interactions

This study aimed to evaluate the effects of the influencing variables on the formation process of the HAZ without the influence of roving integration. In other words, this study determined the influencing variables that had the most significant effect on the HAZ. The starting point for this study was the operating point identified in [19,20]. The significance analysis presented in this paper used a split-plot design (SPD). The obtained understanding of the process formed the basis for the central composite design (CCD) in Section 2.3.

2.2.1. Design of Experiments

According to [25], the best-existing manufacturing process should be used as a starting point for experimental analysis. In [19,20], the initial findings on the integration of rovings in the developed LS machine were obtained. These findings form the first factor level, according to Table 3. The second level is a value in the direction of the presumed improvement. A range that still allows for a clear measurement of the HAZ but does not go too far

beyond the required settings was chosen. In addition, it must be considered that a greater number of tests are required at small distances to prove a factor's significance. Table 3 below lists the factors to be tested for significance in this study with the corresponding level value.

Table 3. Investigated influencing factors with abbreviations, factor levels and adjustability.

Abbreviation	Factor	−1	1	Change
A	κ	Planar	Convex	Before printing
B	$d_{D,o}$	4	2	Before printing
C	h_D	0.8	0.4	Before printing
D	T_D	280	310	Simply via PLC
E	v_D	30	60	Simply via PLC
F	T_{HM3}	190	200	Simply via PLC

The first and second columns list the abbreviations and associated factors. The last column shows how and when each factor can be changed. Factors D, E and F can be easily influenced via the PLC of the LS machine or the G-code, whereas factors A, B and C require more manual adjustment before printing. Factors A and B can only be produced by machining (e.g., turning). Factor C can be adjusted mechanically using a feeler gauge tape. The third column (−1) of Table 3 lists the initial operating points in [19,20]. The penultimate column (1) lists the second level for which an improvement in the target variables is assumed. For the exact quantification of the second level (1), preliminary tests were carried out in [26]. Table 4 lists the parameters to be kept constant in this study.

Table 4. Process and material parameters of the developed LS system selected for the investigations.

Setting	Value
Material	Sintratec PA12 (black)
Mixing ratio	60% Fresh powder/40% used powder
Number of initial layers in sintering phase	20
Sintering temperature, T_O	175 °C
Laser spot diameter	≈0.1 mm
Laser output	1.6 W
Hatch distance	0.1 mm
Scan speed	650 mm/s
Layer thickness	0.1 mm
Energy density per unit area, E_F	0.025 J/mm^2
Inert gas	-
Process chamber temperature	Uncontrollable (≈110 °C)
Difference between hot spot and cold spot in the stable built area (105 mm × 105 mm)	Δ7 K
Heating up time	90 min
Cooling down time	10 h (overnight)
Platform heater	170 °C
Powder emissivity, ε_P	≈0.9
Fibre nozzle emissivity, ε_D	≈0.9 (graphite lacquer)
Emissivity of the surface of the additional heat source (metal plate), ε_{HM3}	≈0.9 (graphite lacquer)

In order to set up an experimental design for the significance analysis intended in this study, the factor level combinations to be carried out must first be determined. As shown in the last column of Table 3, the nozzle curvature, κ, the outer diameter, $d_{D,o}$, and the nozzle distance, h_D, cannot be adjusted during printing but must be set before each print run according to Table 1 (Settings). Complete randomisation of the test sequence requires resetting each factor after each print run. This means that only one specimen can be produced during a print run. For a study of six factors with two factor levels, $2^6 = 64$ prints are required to perform each factor level combination. Due to the comparatively long

heating and cooling down times of the LS machine, only one print per day is realistic. Performing 64 individual prints, therefore, requires 64 working days. For each repetition of all factor level combinations, the effort increases. In addition, the available build volume of the developed LS machine was not optimally used with one specimen per run. This results in the highly inefficient use of build space and the associated high powder consumption. Although unsintered powder can be reused, it does not have the same properties as fresh powder [27–29]. This study uses a full factorial SPD with eight main units and eight subunits to determine the significance of the factors in Table 3. Implementing an SPD allows the $2^3 = 8$ factor level combinations of the simple modifiable factors (D, E and F) specimens to be produced simultaneously in one print run (subunit). The three factors that are difficult to change (A, B and C) are kept constant (main unit). In this way, the effort required to produce the 64 specimens is reduced to eight print runs instead of 64. In addition to time savings, material and energy costs can also be reduced. Further information on the design and evaluation of SPD can be found in [30].

To estimate the required number of experiments, a trade-off must be made between the size of the detectable effect and the experimental effort. The effort should be as great as necessary and as small as possible to prevent waste of resources. The number of individual experiments depends on the required resolution of the detectable effects, $\Delta\mu$, and the standard deviation, σ, of the individual values. The required number of individual experiments can be estimated by the following Equation (4) and is based on [25].

$$N = 2 \times n = 60 \times \left(\frac{\sigma}{\Delta\mu}\right)^2 \quad (4)$$

Since the standard deviation of the tests is unknown, it was estimated by further preliminary tests [26]. The standard deviation for the width b_{HAZ} is 211 µm and 77 µm for the depth t_{HAZ}. In addition, it is known from the preliminary tests that the resulting values for the width b_{HAZ} are between approx. 7500 µm and 1500 µm and between approx. 1900 µm and 250 µm for the depth t_{HAZ} at the planned factor levels. Due to the large range of Δb_{HAZ} = 6000 µm and Δt_{HAZ} = 1550 µm, an effect of 3% of the maximum value is expected to be detected. This corresponds to 225 µm in width and 54 µm in depth. Equation (4), therefore, provides a minimum number of tests of 53 for the width and 122 for the depth of the HAZ. The SPD with six factors on two levels each thus contains 64 individual tests. It can be concluded that two replications per test setting are required. This also results in one replication of the main units, which is needed to estimate the error of the main units. In total, 128 specimens are therefore produced. In addition, the main units are divided into two blocks. By creating blocks, effects that are not considered but are known and cannot be controlled can be considered or eliminated as a block factor. In addition, the order of the blocks and the order of the experiments within the blocks are randomised to prevent unknown trends occurring within a limited time period from distorting the results.

2.2.2. Experimental Procedure

To realise eight subunits, eight specimens were produced in one print run. The specimens were rectangular parts of 20 × 12 × 3 mm^3 (L × W × H) and made of PA12 (Sintratec black). The sample geometry was based on the sample geometry in [19]. The thickness and width of the sample were several times greater than the HAZ so that the heat input took place only within the generated part structure and, thus, the unsintered powder was not melted. The arrangement of the specimens in the powder bed of the developed LS machine is shown in Figure 3 below.

The specimens were positioned 2 mm from each other along the *x*-axis. In addition, adjacent specimens had an offset of 0.5 mm along the *z*-axis (build direction). The HAZ was inserted after 2.5 mm (25th layer) of each part. Since this analysis was only intended to investigate the significance of the factors on the HAZ, no rovings were integrated. The fibre integration unit moved in rapid traverse to the starting position of the path of motion

(red line). From there, the fibre integration unit moved at the feed rate of the fibre nozzle specified in the experimental design. At the end of the motion path, the fibre integration unit returned to its home position at rapid traverse. The settings listed in Table 4 were used to produce the specimens using the developed LS machine.

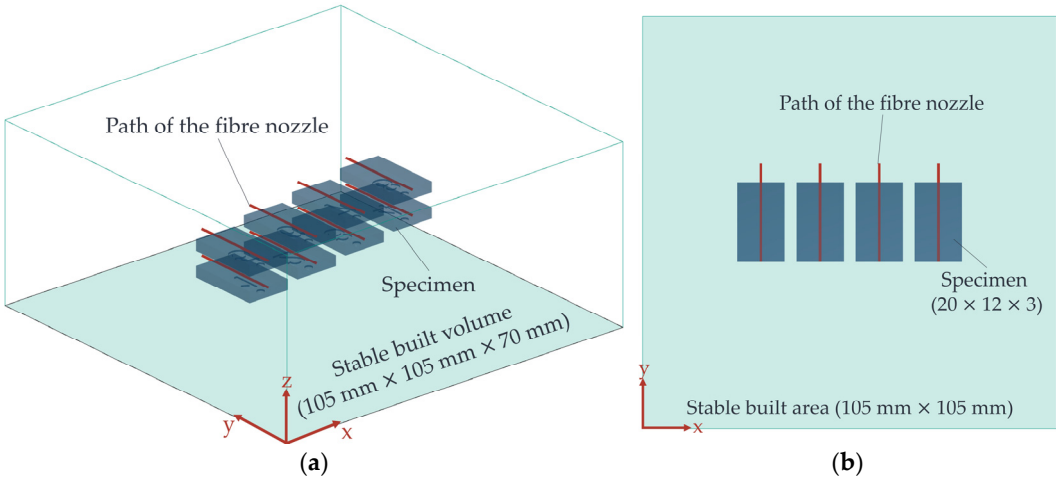

Figure 3. 3D view of the arrangement of the specimens in the built volume of the LS machine (**a**) and a top view (**b**) with the movement path of the fibre nozzle (red lines).

The distance travelled by the fibre nozzle and, therefore, the melted area was longer than the part itself, resulting in a slug at the end faces of the specimens. To determine the width and depth of the HAZ, the specimens were prepared so that the HAZ was visible for evaluation. This was conducted by cutting off the protruding part (slug) of the melted area on the front of the specimens with a scalpel. The HAZ was measured using a microscope (Keyence VHM 7000). The result of a measurement is shown as an example in Figure 4.

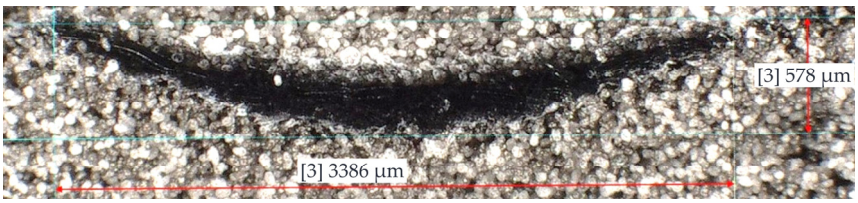

Figure 4. Illustration of the width and depth of the HAZ.

2.2.3. Experiment Evaluation

The SPD was set up and evaluated using Minitab statistical software (2022 Cloud App) to identify the main and interaction effects that had a statistically significant influence on the target variables. The *p*-value is used to describe the result and assess each factor's significance. If the assumption that an effect is zero is referred to as the "zero hypothesis" (H0) and the assumption that an effect is not zero is referred to as the "alternative hypothesis" (H1), the *p*-value represents the smallest possible significance level at which H0 can just be rejected. This means that the effect of a factor has not occurred by chance with a probability of 1-p but actually exists. The *p*-value, therefore, describes the probability that an effect is wrongly assumed to be significant. A smaller *p*-value (for example, $p > 0.001$) indicates greater significance (***) [25,30–32]. The interpretation of *p*-values for a significance level of 5% can be found in Table 5.

To build the experimental model in Minitab, the so-called "sequential forward selection" is used [25]. This starts with a base model, i.e., only the significant main factors. The model is then iteratively extended by the most significant interaction effects [33]. The normal distribution in this analysis was checked using a normal probability plot to evaluate

the resulting model. This can be performed visually by evaluating the residuals. Another requirement of the model is that the input values are independent. As a full factorial SPD was used, this requirement was met and did not need to be checked.

Table 5. Interpretation of the *p*-value for a significance level of 5% (- no indication of difference, * indifferent, ** significant difference, *** highly significant difference).

p	Abbreviation	Interpretation
$p \geq 0.05$	-	No indication of difference
$0.05 > p \geq 0.01$	*	Indifferent, collect more data if possible
$0.01 > p \geq 0.001$	**	Significant difference
$0.001 > p$	***	Highly significant difference

2.3. Study 2: Optimisation of Target Variables

This study aimed to systematically analyse the target variables at an optimal operating point predicted by an FE model using a central composite design (CCD) with the influence of roving integration. The starting points were the main influencing variables evaluated as significant in the first study, and the operating point range was determined by the FE model [21]. The aim was to generate an HAZ that had the lowest possible values for b_{HAZ} and t_{HAZ} so that the roving could still be reliably integrated into the part. At the same time, the process should have a low process time, i.e., a maximum feed rate of the fibre nozzle. The influence of the roving on the HAZ and the overlap of the roving in the part were also investigated. Finally, based on these results, an optimal operating point for a reliable and repeatable roving integration was experimentally derived and discussed.

2.3.1. Design of Experiments

The factors to be investigated were selected based on the results of Study 1. The model to be generated should be simplified by additional assumptions. For the selection of the factor levels, the best experimental point so far should be used, as recommended in [25]. Since no information on this is available, the starting point for this study was estimated using an FE model in COMSOL Multiphysics [21]. To simplify the model to be developed in this study (i.e., to reduce the factors), the smallest possible outer diameter of the fibre nozzle and/or the maximum possible temperature of the fibre nozzle was used, for example.

According to the Stefan–Boltzmann law in Equations (2) and (3), temperature changes have a nonlinear effect on the transferred heat flow. In addition to linear effects, the model to be created should also describe quadratic effects. For this reason, a CCD is used to describe both linear and nonlinear effects. An α of $\sqrt{2}$ is chosen for the star points to ensure repeatability. By repeating the test in the centre point several times, the variance can also be determined more precisely. The results obtained for each test point can be approximated to the measured results using a regression model. For a two-factor model, the polynomial function is presented in the following form in Equation (5).

$$f(x, y) = a_0 + a_1x + a_2y + a_3xy + a_4x^2 + a_5y^2 + a_6x^2y^2 \quad (5)$$

To obtain orthogonal blocks, five centre points per block were selected [31,34]. Each combination of factor levels and their respective centre points were produced within one print, thus forming one block. The experimental order within four blocks was randomised using Minitab software (2022 Cloud App).

In addition to the experimental design described above, the influence of the rovings on the HAZ was analysed. For this purpose, the central point was repeated five times without the influence of the roving, and the results were compared with the FE model in [21].

2.3.2. Experimental Procedure

The arrangement of the specimens in the powder bed, the numbering of the specimens and the determination of the width and depth of the HAZ were the same as in Study 1. The

geometry was 60 × 15 × 3 mm^3 (L × W × H). Only the sample length was increased to 60 mm. The reason for this is that the developed LS machine can reliably process rovings with a minimum length of 55 mm. However, since the roving is difficult to distinguish from the surrounding matrix when viewing from the front, the specimen is cut open with a scalpel, as shown in Figure 5b, to measure the roving overlap [26].

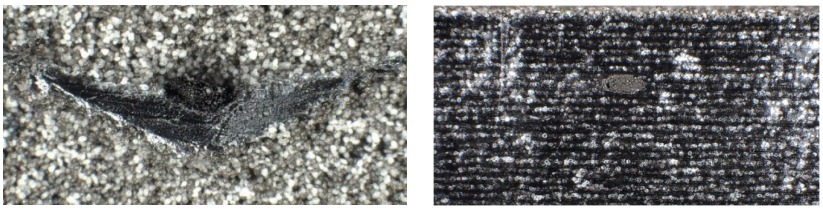

(**a**) (**b**)

Figure 5. Comparison of a cut open HAZ (**a**) and a cut open specimen (**b**).

To determine the roving overlap, the total part thickness is first determined. Based on the known total number of powder layers per part n_{tot} = 30, the thickness per layer h_S^* (≈0.095 mm) can thus be determined—see Figure 6. This layer thickness h_S^* is necessary since the part will shrink during cooling. In addition, the roving overlap h_R can be determined from the known integration layer of the roving at n_{FI} = 25. The roving overlap is compared to the set powder layer thickness during printing and/or the movement level of the recoater at h_S (=0.1 mm) and should be ideally $h_R < h_S$.

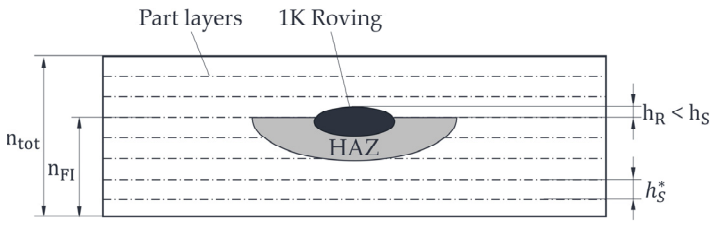

Figure 6. Schematic representation for calculating the roving overlap within a specimen.

The same machine settings were used for this study, as shown in Table 4. The roving used was a coated 1K roving (67 tex, HTA40) from Teijin Limited. To ensure proper fibre–matrix bonding, the roving used had a thermoplastic-compatible polymer dispersion (PERICOAT AC250) as a coating material [35]. The coating content was 5% [36].

2.3.3. Experiment Evaluation

The principle of sequential forward selection was applied to generate a suitable model, as in Study 1. In this observation, a significance level of 10% was chosen, from which a term was included in the model. It was also checked whether adding a term improved the coefficient of determination, R^2. The R^2 provides information on the degree to which the dependent variables (target variables) can be described by the independent variables (factors) under consideration. For an error-free description of the target variables, R^2 is close to or equal to 1. The model set up with this methodology contained both the linear and the quadratic main effects according to Equations (2) and (3) for the model of width and depth. Using MATLAB, the results are presented and interpreted using 3D plots and contour plots. To identify a maximum feed rate value for the fibre nozzle, an optimisation direction was derived from the results of the CCD and verified experimentally with additional specimens.

3. Results and Discussion

3.1. Main Influencing Variables and Interactions

Figures 7 and 8 show the normal probability plot of the residuals for the target variable width and depth, respectively.

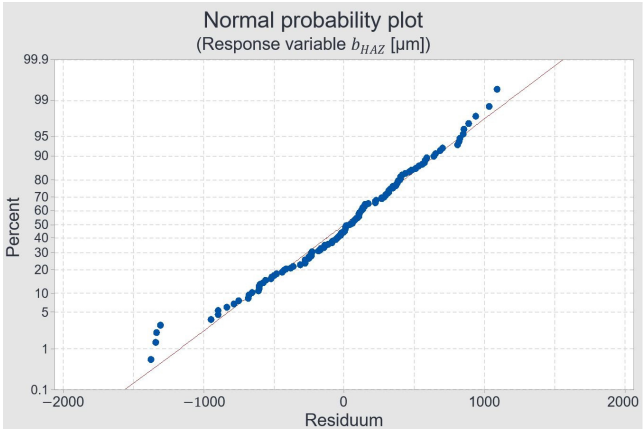

Figure 7. Normal probability plot for the width of the HAZ.

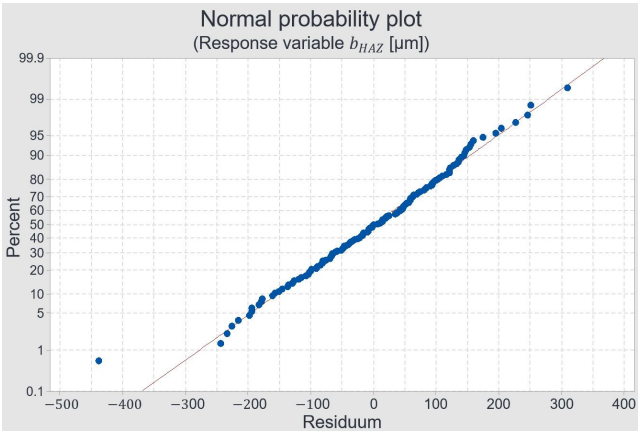

Figure 8. Normal probability plot for the depth of the HAZ.

It can be seen that the residuals for both response variables approximately follow a straight line and show no patterns. Only the depth shows a slight outlier in the lower left-hand corner, which is considered negligible. The residuals are, therefore, derived from a normally distributed population [25].

Table 6 shows the results of the significance analysis with the *p*-value for the main and interaction effects included in the model for the width of the HAZ.

The first column lists the factors and interactions, the second column the associated effects, the third column the *p*-values and the fourth column the order of significance for the factors and interactions. All interactions not presented had a *p*-value > 0.05 and were, therefore, not significant. The magnitude of the calculated effects for the main effects was between 246.2 and 2247.3 µm. The nozzle diameter (B) had the most significant impact on the width of the HAZ. On the other hand, the temperature of the additional heat source (F) played a minor role. A highly significant difference could only be demonstrated for the linear main effects, except for the temperature of the additional heat source and the interaction between the nozzle curvature and the nozzle diameter. This is also reflected in the magnitude of the effects of these. In addition, the *p*-value for "blocks" was 0.549, indicating no significant difference between the first and second repetition of the experiments. Thus, it can be assumed that the experimental conditions did not change much. Table 7 shows the results of the significance analysis for the main and interaction effects included in the model for the depth of the HAZ.

Table 6. Results of the SPD with the effects of the factors and interactions on the width of the HAZ (- no indication of difference, * indifferent, ** significant difference, *** highly significant difference).

Factor	Effect (µm)	*p*-Value	Significance
Block	-	0.549	-
A	−748.8	0.000	***
B	2247.3	0.000	***
C	−549.3	0.000	***
AB	−658.1	0.000	***
D	748.1	0.000	***
E	−958.2	0.000	***
F	246.2	0.016	*
BD	−145.2	0.150	-
AEF	−279.5	0.006	**
BDF	−304.8	0.003	**
BEF	−287.7	0.005	**
DEF	−226.9	0.026	*
ACDF	−309.4	0.003	**
ABCDE	−263.3	0.010	*
ABCDF	208.6	0.040	*
ABDEF	−218.9	0.031	*

Table 7. Results of the SPD with the effects of the factors and interactions on the depth of the HAZ (- no indication of difference, * indifferent, ** significant difference, *** highly significant difference).

Factor	Effect (µm)	*p*-Value	Significance
Block	-	0.226	-
A	−154.0	0.000	***
B	330.3	0.000	***
C	−234.2	0.000	***
AB	−127.8	0.000	***
AC	71.7	0.013	*
D	173.9	0.000	***
E	−270.6	0.000	***
F	22.2	0.350	-
BD	2.2	0.927	-
BE	−51.7	0.031	*
CF	−49.5	0.038	*
DE	−62.0	0.010	*
AEF	−56.1	0.019	*
BDF	−83.3	0.001	**
ABEF	−52.7	0.028	*
ACDF	−55.0	0.022	*

For depth, all unlisted interactions also had a p-value > 0.05 and were, therefore, insignificant. The magnitude of the calculated effects for the main effects as between 22.2 and 330.3 µm. The impact on depth was, thus, significantly smaller than on the width. This is also reflected in the shape of the HAZ, which was significantly wider than deep for each specimen—see Figure 5. The nozzle diameter (B) also influenced the depth the most. Only the main influencing factors and the interaction (AB) between the nozzle curvature (A) and the nozzle diameter (B) had a highly significant influence on the depth. The temperature of the additional heat source (F) had no effect. The p-value of 0.226 for the blocks was significantly lower than for the width but was also insignificant. Therefore, there is no indication of a significant change in the environmental influences over the test period either. Considering the two tables on the width and depth of the HAZ, the following key statements on the main effects can be summarised:

- The change from a planar to a convex fibre nozzle (A) causes a reduction in the width and depth of the HAZ on average. Accordingly, a planar fibre nozzle should be used for a higher width and a convex fibre nozzle for a smaller width of the HAZ;
- The effect of the nozzle diameter (B) for b_{HAZ} was 2247.31 µm and for the depth t_{HAZ} 330.30 µm. This means that, ceteris paribus, for every millimetre increase in the nozzle diameter, the HAZ becomes, on average, 1123.65 µm wider and 165.15 µm deeper. This is also in the expected direction since, according to Equation (3), the transferred heat energy increases with an increasing surface area. Therefore, for small values of b_{HAZ}, the smallest possible nozzle diameter should be used;
- The effects of the nozzle distance (C) were −549.25 µm for the width and −234.17 µm for the depth of the HAZ. Increasing the nozzle distance, therefore, causes a reduction in b_{HAZ} and t_{HAZ}. This effect seems logical and can be explained by increasing the nozzle distance using Equation (3) and the associated reduced heat flux;
- The effects of the nozzle temperature (D) on the depth and width were 748.13 µm and 173.89 µm, respectively. An increase in temperature by 1 K, ceteris paribus, causes an average increase in b_{HAZ} by 24.94 µm and 4.35 µm for t_{HAZ}. This effect can also be explained by Equation (3);
- The effect of the feed rate of the fibre nozzle (E) was −958.22 µm for b_{HAZ} and −270.58 µm for t_{HAZ}. Thus, ceteris paribus, increasing the feed rate reduces the width of the HAZ by 31.94 µm and the depth by 9.02 µm on average. The direction of the effect can be explained by the shorter heat transfer time with an increasing speed. The feed rate is suitable for achieving a deeper HAZ without becoming significantly wider. However, this means a speed reduction. As a high process speed is required, a compromise must be found for this trade-off;
- While the other main factors were rated "highly significant", the temperature of the additional heat source (F) was rated "indifferent, collect more data if possible" for width and "no indication of difference" for depth. However, the additional heat source seems to have had a positive effect. This statement should be interpreted cautiously since the effect is not statistically significant. Varying the temperature of the additional heat source over a broader range may, therefore, produce a significant effect but is not recommended according to [20] (premature crystallisation of the part).

The highly significant interaction represents the interaction (AB). The interaction effect was −658.1 µm for the width and −127.8 µm for the depth. For better interpretation, a graphical interpretation was made—see Figures 9 and 10. In both figures, in the bottom left, the fibre nozzle curvature (A) is plotted on the *x*-axis versus the dimensions of the HAZ on the *y*-axis. The red line represents the fibre nozzle with $d_{D,o}$ = 4 mm, and the blue line represents the fibre nozzle with $d_{D,o}$ = 2 mm. It can be seen from Figure 9 that the width and depth behave almost identically, except for the scaling. This indicates that the interaction effect was similar for width and depth. The blue line is nearly horizontal, whereas the red line has a noticeable downward slope. For the fibre nozzle with $d_{D,o}$ = 2 mm diameter, there is almost no difference between a planar fibre nozzle and a convex fibre nozzle. The nozzle curvature, therefore, has virtually no effect on the HAZ characteristics for the smaller fibre nozzle. However, for the fibre nozzle with $d_{D,o}$ = 4 mm, a convex fibre nozzle causes a smaller width of the HAZ than a planar fibre nozzle. The top right diagram shows the same situation. Here, however, the colours of the lines represent the nozzle curvature, and the nozzle diameter is plotted on the *x*-axis. The nozzle diameter, therefore, has a much more significant influence on a planar fibre nozzle than on a convex fibre nozzle.

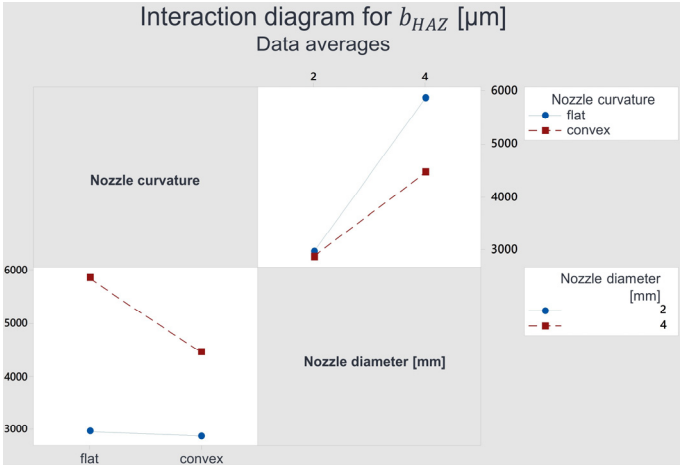

Figure 9. Interaction diagram for the interaction AB for the width of the HAZ.

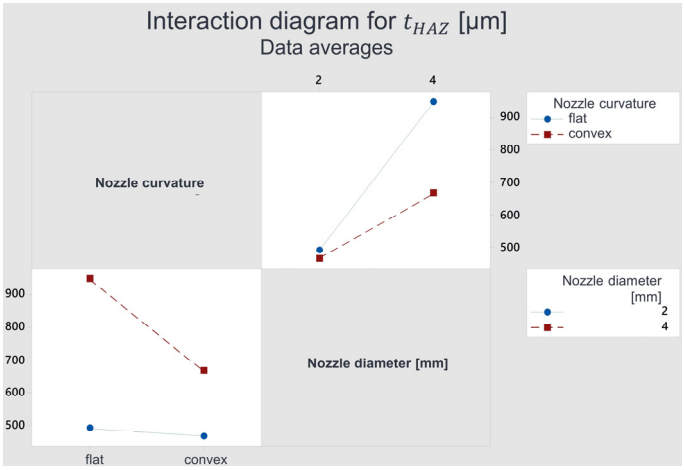

Figure 10. Interaction diagram for the interaction AB for the depth of the HAZ.

3.2. Optimisation of Target Variables

To simplify this analysis, the nozzle diameter, nozzle curvature, nozzle distance and temperature of the additional heat source were kept constant. According to Study 1, the nozzle diameter should be as small as possible to obtain a small value of b_{HAZ}. As in Study 1, an outer diameter of 2 mm was used in this analysis. This value represents the smallest diameter that can be manufactured. In addition, a planar nozzle was used since the influence of the nozzle curvature was negligible with decreasing nozzle diameters, according to the findings from Study 1. As mentioned in Study 1, a nozzle spacing of 0.4 mm resulted in increased powder adhesion to the fibre nozzle. In preliminary tests, this value was increased to 0.6 mm. At this nozzle distance, rovings can be repeatedly integrated without powder adhesion [26]. According to Study 1, increasing the nozzle distance leads to widening the HAZ. Since this effect was not desired, the nozzle distance was kept constant at 0.6 mm. The temperature for the additional heat source at the fibre integration unit was set to 185 °C to avoid the premature crystallisation of the part and, thus, curling during roving integration. Therefore, the nozzle temperature and the nozzle feed rate remained as factors in this analysis. The result was a two-dimensional model.

For the analysis of the nonlinear effects, the predicted operating point from the FE model in COMSOL Multiphysics formed the starting point—see in [21]. In this simulation-based optimisation, it was assumed that the depth of the HAZ must be at least as thick as the roving thickness to place the roving completely into the generated HAZ and, thus, avoid contact between the roving and the recoater. With a measured roving thickness (1K) of 0.4 mm, the FE model predicted a nozzle feed rate of approx. 110 mm/min at a nozzle

temperature of 345 °C. The factor levels for the CCD listed in Table 8 were used to analyse the region around this identified point.

Table 8. Factor levels used for the CCD with abbreviations.

Factor	$-\alpha$	-1	0	1	α
T_D (°C)	335	338	345	352	355
v_D (mm/min)	92	99	116	133	140

Equation (6) shows the regression function generated by Minitab to describe the width of the HAZ.

$$b_{HAZ} = 222,195 - 1275T_D - 41.8v_D + 1.878T_D^2 + 0.1377v_D^2 \quad (6)$$

The standard error of the regression was 108.54 µm. The model can, therefore, predict the width values with an accuracy of 108.54 µm. The coefficient of determination was R^2 = 0.8051 and was close to one. The model can, thus, explain a large part of the variance. The model is illustrated in Figure 11 as a surface response (a) and contour plot (b) for interpretation. Figure 11 shows that the HAZ's width decreases with a decreasing nozzle temperature and increasing nozzle feed.

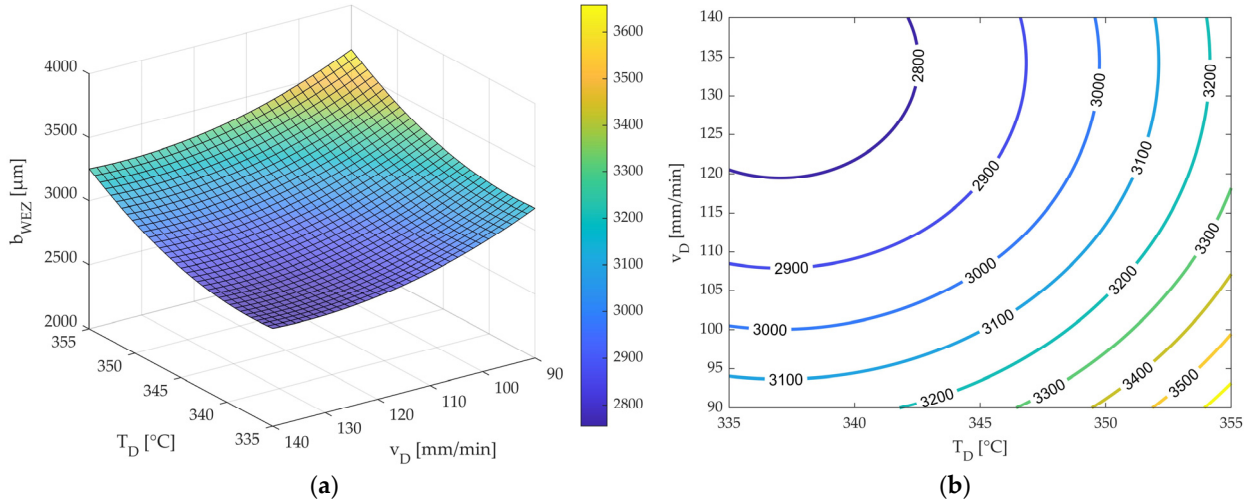

Figure 11. Response surface plot (**a**) and contour plot (**b**) for the width of the WEZ with the influence of roving integration.

It can be seen that the effect of nozzle temperature increased with higher nozzle temperatures. This can be explained by the fact that heat conduction is the dominant effect on the amount of heat transferred, but heat radiation also has an influence. Since heat radiation increases proportionally with the fourth power of temperature according to Equation (3), this can explain the increasing effect of nozzle temperature with increasing temperature. Since the heat flow is a function of the heat energy and the heat transfer period, a higher feed rate will result in a lower heat flow [23]. The effect of the nozzle feed decreased with an increasing feed rate. The surface response with the narrowest HAZ can be seen in the contour diagram (b) in the top left. The nozzle temperature, in this case, was between approx. 335 °C and 342 °C with a nozzle feed rate between approx. 135 °C and 140 mm/min. For this range, a width of the HAZ below 2700 µm and above 2600 µm was predicted.

Equation (7) shows the regression function generated by Minitab to describe the depth of the HAZ with the influence of the roving integration.

$$t_{HAZ} = 39,969 - 224.5T_D - 18.14v_D + 0.33T_D^2 + 0.0651v_D^2 \quad (7)$$

The standard error of the regression, S, for the depth of the HAZ was also low at 35.6891 µm. Therefore, the predicted deviation from the actual value was only 35.6891 µm. The coefficient of determination of R^2 = 0.7178 was lower than that for the width model, but it is acceptable. The surface response and contour plot for t_{HAZ} is shown in Figure 12.

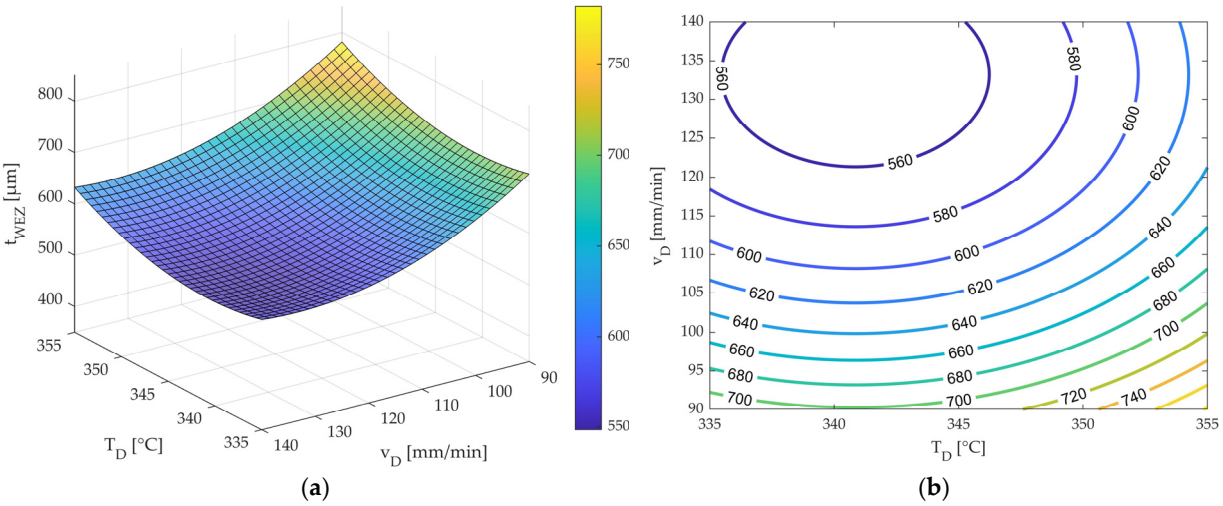

Figure 12. Response surface plot (**a**) and contour plot (**b**) for the depth of the WEZ with the influence of roving integration.

It can be seen that the depth of the HAZ also decreased with the decreasing nozzle temperature and increasing nozzle feed rate. This is also consistent with the findings of Study 1. In addition, an increasing effect with an increasing nozzle temperature and decreasing nozzle feed rate can also be seen for the depth. This effect can be attributed to the same causes as for the width.

The optimum range for depth is also shown at the top left of the contour diagram (b). In this case, the point was at a nozzle temperature between 335 °C and 345 °C and a feed rate between 130 mm/min and 140 mm/min. For this range, the depth of the HAZ was predicted to be below 540 µm and above 520 µm.

To investigate the roving integration's influence on the HAZ's width and depth, the same factor levels were chosen in the FE model as in Table 8 [21]. Equation (8) shows the regression function for the FE model results to describe the HAZ depth without the influence of the roving.

$$t_{HAZ} = 63,424 - 369T_D - 1v_D + 0.541T_D^2 + 0.0008v_D^2 \quad (8)$$

In addition, the central composite design's central point without roving integration was repeated five times on the developed LS machine to quantify the influence of roving integration on the HAZ experimentally. In the following Figure 13a, the surface response plot according to Equation (8) of the FE model (lower surface response plot, without the influence of the roving) and of Equation (7) (upper surface response plot, with the influence of the roving) were compared. Figure 13b shows the experimental comparison of the central point with and without roving integration. It can be seen that with roving integration, the depth of the HAZ was more significant compared to without roving integration. In addition, Figure 13b shows that roving integration mainly affects the depth (+100 µm) and only marginally the width of the HAZ (+32 µm). The overlapping of the scatter bars also shows this. The reason for the increase in depth is the heat transferred from the heated

fibre nozzle to the roving. The intrinsic heat generated by the roving caused additional melting, increasing the HAZ's depth by an average of 110 µm.

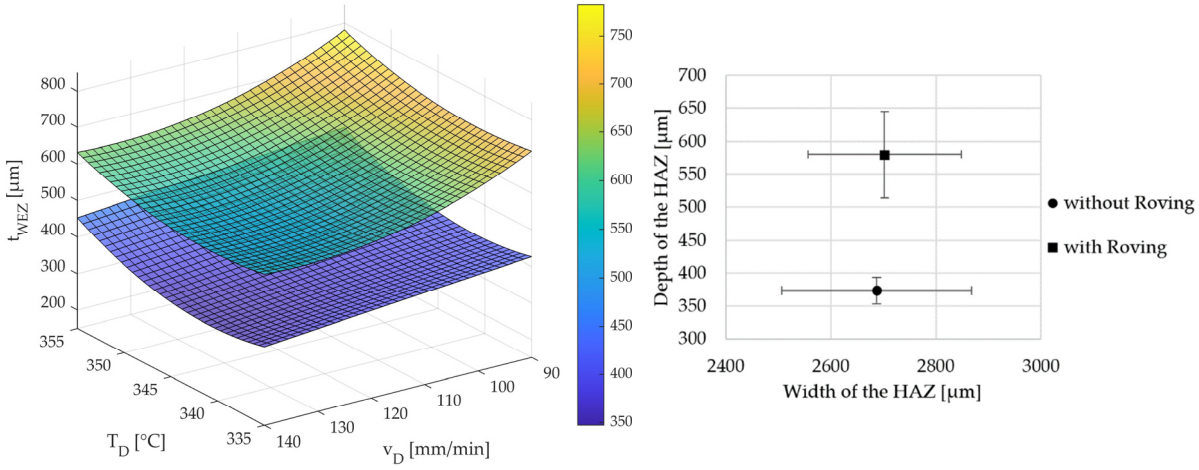

(**a**) (**b**)

Figure 13. Comparison of the response surface plots with (CCD) and without (FE model) roving influence on HAZ depth (**a**). Comparison of the experimental results for the HAZ at the central point with and without roving integration (**b**).

For the evaluation of the roving overlap above the part level in which the roving was integrated (process reliability), no significant influence of the nozzle feed was found on the nozzle feed rate in the range between 92 mm/min and 140 mm/min. For this reason, additional specimens were used to analyse the nozzle feed rate limits. A nozzle temperature of 345 °C was set for these specimens, and the nozzle feed rate was varied. The additional feed rates were 160, 180, 200, 220, 240 and 300 mm/min. Each setting was repeated twice. In addition, to obtain comparability between the specimens, only the specimens from the CCD using a nozzle temperature of 345 °C were used. The results for the measured roving overlaps, the level of movement of the recoater (red) and a linear trend line (black) for the measured measuring points are shown in Figure 14a. Figure 14b also indicates the rovings' orientation in the selected specimens' component.

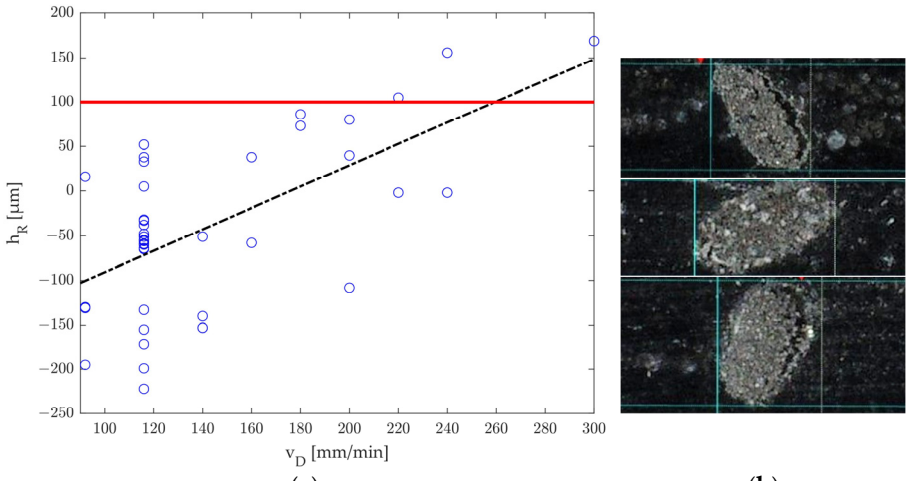

(**a**) (**b**)

Figure 14. Influence of nozzle feed rate on roving overlap (**a**) and uncontrolled roving orientation within the specimen (**b**). The red line in (**a**) indicates the layer thickness during printing.

The level of movement of the recoater in Figure 14a was 100 µm and corresponded to the set layer thickness during printing. Figure 14a also shows the variation of the

measured values. However, an increasing nozzle feed rate leads to the roving sinking less into the HAZ, resulting in an increased risk of the recoater hitting the roving or possibly entangling it. Although there were fewer measured values for the specimens with feed rates above 140 mm/min, three values (i.e., 25% of these specimens) exceed the 100 µm limit. Looking at Figure 14b, it is noticeable that the shape and orientation of the rovings varied significantly among the specimens. While in some specimens, the fibre was flat and wide, in others, it was high and narrow. Orientation is, therefore, a strong scattering factor that significantly influences successful fibre integration.

In particular, the random orientation of the rovings significantly influences the roving overlap and, thus, the process reliability. For this reason, process limits are defined, which result from the tests and the relationships previously described. On the one hand, it can be noted that as the nozzle feed rate increased and the nozzle temperature decreased, the roving sunk less deep into the part. This increases the risk of the recoater getting stuck on and entraining the roving. In addition, it was observed that this also increased the risk of powder adhering to the nozzle, leading to an abortion of the printing process. Powder sticking to the nozzle occurred at 335 °C at 160 mm/min and 345 °C at 200 mm/min. In the CCD study, the range between 335 °C and 355 °C for the nozzle temperature and between 92 mm/min and 140 mm/min for the nozzle feed rate were examined in more detail. No disturbances occurred during the production of 52 specimens, which is the reason to assume that a process-reliable fibre integration takes place in this range.

Possible reasons for the lower coefficients of determination, as well as the uncontrolled roving orientation, are listed below:

- The entire structure of the fibre integration unit remains in the process chamber of the developed LS machine during the printing time, which also causes it to heat up. Due to the thermal expansion of the fibre integration unit, the manually set values (e.g., nozzle distance) can change compared to the cold state of the system and thus contribute to scatter in the results. In addition, the feed spindles for positioning the fibre integration unit also expand thermally. Thermal expansion of these spindles will lead to increased errors and, therefore, changed values of the nozzle feed rate;
- The accuracy of the PLC temperature setting is ±1 °C. These deviations can also contribute to scatter in the measurement results;
- The inner diameter of the fibre nozzle is larger than the thickness of the roving. The result is an increased play of the roving inside the fibre nozzle, and this play can lead to the uncontrolled placement of the roving in part;
- Other influences, such as the position of the specimens in the powder bed, the powder's ageing condition and the rovings' delivery condition, can lead to a deviation in the results.

3.3. Determination of an Optimal Operating Point

All target parameters must be considered to determine an optimal operating point for the developed LS machine. The nozzle temperature and the nozzle feed rate settings have the opposite effect on the different target variables. A high nozzle feed rate is beneficial for the width and depth of the HAZ and the processing speed. In addition, a decreasing nozzle temperature leads to a reduction in the width and depth of the HAZ. On the other hand, a high nozzle temperature and a low nozzle feed rate are favourable for process reliability. The CCD identified a range of 335 °C to 342 °C at a nozzle feed rate of 135 mm/min to 140 mm/min for the width and a range of 335 °C to 345 °C at a nozzle feed rate of 130 to 140 mm/min for the depth as optimal. Reducing the nozzle temperature or increasing the nozzle feed rate will result in a further reduction, but these values should not be exceeded for process safety reasons. Since the nozzle feed rate increase will improve all three remaining target values, the process limit of 140 mm/min was selected to optimise this factor. The nozzle temperature does not affect the processing speed, but a reduction will also reduce the HAZ. Since the effect of the nozzle temperature seems small in the range between 335 and 345 °C, 340 °C was selected here instead as the limit value to ensure a

higher process reliability. The optimised point for process speed and HAZ size, considering process reliability, is the factorial combination of a nozzle temperature of 340 °C and a nozzle feed rate of 140 mm/min. According to the model, the expected width and depth of the HAZ for this setting were 2638.72 µm and 523.36 µm, respectively. An overview of all settings for an optimum operating point is given in Table 9.

Table 9. Identified operating points evaluated as optimal for reproducible and process-reliable roving integration.

Operating Points	
κ	Planar
$d_{D,o}$ (mm)	2
h_D (mm)	0.6
T_D (°C)	340
v_D (mm/min)	140
T_{HM3} (°C)	190

The following approaches can be used to increase the process reliability and process time in the future:

- For a more controlled orientation of the rovings in the part, the inner diameter can be made smaller or adapted to the shape of the roving;
- Additional twisting of the rovings before coating could produce a rounder shape and, thus, in combination with an adapted inner diameter of the fibre nozzle, result in a higher deposition accuracy in part.

4. Conclusions

Additive manufacturing of CCFRP parts with the LS machine developed aims to combine the process-specific advantages of the LS process with the advantages of continuous fibre reinforcement. With this LS machine, in the future, complex shapes and near-net-shape functional parts with promising basic properties (matrix) will be able to be reinforced in a load-path-oriented manner with the help of continuous fibres. Thus, CCFRP parts can be produced economically without support structures and cost, as well as time-consuming post-processing steps. The starting point of this study was an initial starting point from previous research work, which enables roving integration but is particularly unfavourable with regard to the processing time and the achievable FVC. High process times are required to integrate rovings, which results in inefficient production. In addition, the HAZ at the initial starting point is too large, which means that rovings can only be placed at a considerable distance from the part edges. The FVC and the associated mechanical properties of the CCFRP parts can thus only be increased slightly. To systematically increase the FVC and the mechanical properties in future research work, a comprehensive understanding of the process was derived in this paper. Based on this, the LS process with continuous fibre integration was optimised in terms of process time, process reliability and the shape of the HAZ. The essential core conclusions of this study are summarised in the following points:

- In the first study of this paper, both the law of heat conduction, as well as the law of heat radiation, as in Equations (2) and (3), can explain the findings on the effects of the influencing variables on the target variables in a first approximation;
- To obtain the narrowest but deepest possible HAZ, a small nozzle diameter and a small nozzle distance should be selected. The nozzle curvature should be convex for a large diameter. For a small diameter, a planar nozzle can be used instead. Nozzle temperature has a balanced effect on the width-to-depth ratio of the HAZ. A low feed rate is beneficial to the shape of the HAZ. However, since a high process speed is also required, there is a trade-off;
- In the second study, the target variables were analysed in more detail with the help of a CCD. The coefficient of determinations for the width with $R^2 = 0.8051$ and the

depth with R^2 = 0.7178 were close to 1. The developed regression models, therefore, describe the target variables quite well. Possible reasons for the lower coefficients of determination are thermal expansion of the fibre integration unit, deviations in temperature setting via the PLC, play between the roving and the inner diameter of the fibre nozzle, as well as scattering effects, due to the laser-sintering process (material, the position of specimens in the powder bed, etc.);

- With the help of this study, an increase in the nozzle feed rate of 233% up to 140 mm/min was demonstrated for the integration of rovings. Thus, more economical production of CCFRP parts in the developed LS machine is now possible. The width and depth of the HAZ were reduced to b_{HAZ} = 2638.72 µm (−56%) and t_{HAZ} = 523.36 µm (−44%), respectively, so that rovings can now be integrated closer to the part edges and, thus, the FVC can be set higher. This study, therefore, provides optimised operating points for future research;
- Limitations, nevertheless, arise in the processing time. Although an increase in the process time of 233% appears to be high, the manufacturing time for CCFRP parts with a high FVC can be pretty high. A lower FVC is required for CCFRP parts with a local reinforcement at highly stressed areas. For such parts, the manufacturing time increases only slightly. Furthermore, it must be considered that rovings can be placed close to part edges, but it must be expected that melted material or the HAZ protrudes from the part surface. For a homogeneous surface, the protruding material must be removed.

Future research will address the systematic increase of the FVC and the associated mechanical properties. To increase the FVC, in addition to placing rovings in the vicinity of part edges, the relative roving distances in the vertical (build-up direction in the LS process) and horizontal (within the powder bed surface) directions are to be considered in particular. Tensile specimens will then be produced following ISO 527 to illustrate the mechanical properties and, finally, the potential of this LS process with continuous fibre integration. Furthermore, the influence of the nozzle temperature on the roving properties is to be investigated. Possible fields of application for this LS process for CCFRP parts arise in production engineering. For example, lightweight tools specially adapted for the application of industrial robots (gripper fingers with internal air channels for parallel jaw grippers, suction grippers with integrated springs) can be produced economically and time-efficiently, thus reducing the moving masses and energy requirements.

Author Contributions: Conceptualisation and methodology, M.B.; validation, formal analysis and investigation, M.B. and L.V.; data curation, L.V.; writing—original draft preparation, M.B.; writing—review and editing, M.B., M.F. and J.F.; visualisation, M.B.; supervision, J.F.; project administration, M.F. and M.B. All authors have read and agreed to the published version of the manuscript.

Funding: This research received no external funding.

Institutional Review Board Statement: Not applicable.

Informed Consent Statement: Not applicable.

Data Availability Statement: Not applicable.

Acknowledgments: The authors would like to thank the Karlsruhe Research Factory of the Karlsruhe Institute of Technology for the opportunity to carry out the results of this paper. Furthermore, we acknowledge support by the KIT-Publication Fund of the Karlsruhe Institute of Technology.

Conflicts of Interest: The authors declare no conflict of interest.

References

1. Schlüsseltechnologie Leichtbau. Available online: https://www.bmwi.de/Redaktion/DE/Schlaglichter-der-Wirtschaftspolitik/2019/05/kapitel-1-6-schluesseltechnologie-leichtbau.html (accessed on 2 May 2020).
2. Schürmann, H. *Konstruieren mit Faser-Kunststoff-Verbunden*, 2nd ed.; Springer: Berlin, Germany, 2007. [CrossRef]

3. Baumann, F.; Sielaff, L.; Fleischer, J. Process Analysis and Development of a Module for Implementing Continuous Fibres in an Additive Manufacturing Process. In Proceedings of the SAMPE Europe Symposium 2017, Stuttgart, Germany, 14–16 November 2017.
4. Vaneker, T. Material extrusion of continuous fiber reinforced plastics using commingled yarn. *Procedia CIRP* **2017**, *66*, 317–322. [CrossRef]
5. Matsuzaki, R.; Ueda, M.; Namiki, M.; Jeong, T.-K.; Asahara, H.; Horiguchi, K.; Nakamura, T.; Todoroki, A.; Hirano, Y. Three-dimensional printing of continuous-fiber composites by in-nozzle impregnation. *Sci. Rep.* **2016**, *6*, 23058. [CrossRef] [PubMed]
6. Yang, C.; Tian, X.; Liu, T.; Cao, Y.; Li, D. 3D printing for continuous fiber reinforced thermoplastic composites: Mechanism and performance. *Rapid Prototyp. J.* **2017**, *23*, 209–215. [CrossRef]
7. Akhoundi, B.; Behravesh, A.H.; Saed, A.B. Improving mechanical properties of continuous fiber-reinforced thermoplastic composites produced by FDM 3D printer. *J. Reinf. Plast. Compos.* **2019**, *38*, 99–116. [CrossRef]
8. Bettini, P.; Alitta, G.; Sala, G.; Di Landro, L. Fused deposition technique for continuous fiber reinforced thermoplastic. *J. Mater. Eng. Perform.* **2017**, *26*, 843–848. [CrossRef]
9. Dickson, A.N.; Barry, J.N.; McDonnell, K.A.; Dowling, D.P. Fabrication of continuous carbon, glass and Kevlar fibre reinforced polymer composites using additive manufacturing. *Addit. Manuf.* **2017**, *16*, 146–152. [CrossRef]
10. Friedrich, K.; Walter, R. (Eds.) *Structure and Properties of Additive Manufactured Polymer Components*; Woodhead Publishing: Cambridge, UK, 2020.
11. Karalekas, D.; Antoniou, K. Composite rapid prototyping: Overcoming the drawback of poor mechanical properties. *J. Mater. Process. Technol.* **2004**, *153–154*, 526–530. [CrossRef]
12. Goh, G.D.; Yap, Y.L.; Agarwala, S.; Yeong, W.Y. Recent Progress in Additive Manufacturing of Fiber Reinforced Polymer Composite. *Adv. Mater. Technol.* **2019**, *4*, 1800271. [CrossRef]
13. Lu, Y.; Han, X.; Gleadall, A.; Chen, F.; Zhu, W.; Zhao, L. Continuous fibre reinforced Vat photopolymerisation (CONFIB-VAT). *Addit. Manuf.* **2022**, *60*, 103233. [CrossRef]
14. Schmid, M. *Laser Sintering with Plastics: Technology, Processes, and Materials*; Hanser: München, Germany, 2018. [CrossRef]
15. Fischer, M.; Josupeit, S. Material Properties of Additive Manufactured Polymer Parts. In Proceedings of the Inside 3D Printing Conference and Expo, Berlin, Germany, 10–11 March 2014.
16. Gebhardt, A. *Additive Fertigungsverfahren: Additive Manufacturing und 3D-Drucken für Prototyping–Tooling–Produktion*, 5th ed.; Hanser: München, Germany, 2016.
17. Lasersintern–Optimal für Hohen Durchsatz. Available online: https://www.industrial-production.de/additive-fertigung/lasersintern-fuer-hohen-durchsatz-898725.htm (accessed on 23 November 2021).
18. Breuninger, J.; Becker, R.; Wolf, A.; Rommel, S.; Verl, A. *Generative Fertigung mit Kunststoffen: Konzeption und Konstruktion für Selektives Lasersintern*; Springer: Berlin, Germany, 2013. [CrossRef]
19. Baranowski, M.; Beichter, S.; Griener, M.; Coutandin, S.; Fleischer, S. Additive Manufacturing of Continuous Fibre-Reinforced Plastic Components by a Novel Laser-Sintering Process. In Proceedings of the SAMPE Europe Conference 2021, Baden/Zurich, Switzerland and online, 29–30 September 2021.
20. Baranowski, M.; Basalla, F.; Friedmann, M.; Fleischer, J. Thermal Analysis of a Novel Laser Sintering Machine for Additive Manufacturing of Continuous Carbon Fiber Reinforced Polymer Parts. *SSRN Electron. J.* **2023**, 1–39. [CrossRef]
21. Spintzyk, A. Simulative and Experimental Investigation of the Heat-Affected Zone for Continuous Fiber Integration in the Laser Sintering Process. Bachelor's Thesis, Karlsruhe Institute of Technology, Karlsruhe, Germany, 2022.
22. Burchard, B.; Baranowski, M.; Fleischer, J. Verfahren und Vorrichtungen zur Integration funktionaler Fasern in ein Werkstück beim Selektiven-Laser-Sintern (SLS). Official File Number: DE 10 2020 125 628.0, 30 September 2020. Patent registration.
23. Stephan, P.; Kabelac, S.; Kind, M.; Mewes, D.; Schaber, K.; Wetzel, T. (Eds.) *VDI-Wärmeatlas*, 12th ed.; Springer: Berlin, Germany, 2019. [CrossRef]
24. Bernhard, F. (Ed.) *Handbuch der Technischen Temperaturmessung*, 2nd ed.; Springer: Berlin, Germany, 2014. [CrossRef]
25. Kleppmann, W. *Versuchsplanung: Produkte und Prozesse Optimieren*, 10th ed.; Hanser: München, Germany, 2020. [CrossRef]
26. Völger, L. Design of Experiments (DoE) to Optimize an SLS-System for Additive Manufacturing of Plastic Components with Continuous Fibers. Bachelor's Thesis, Karlsruhe Institute of Technology, Karlsruhe, Germany, 2022.
27. Shi, Y.; Li, Z.; Sun, H.; Huang, S.; Zeng, F. Effect of the properties of the polymer materials on the quality of selective laser sintering parts. *Proc. IMechE* **2004**, *218*, 247–252. [CrossRef]
28. Goodridge, R.D.; Hague, R.J.; Tuck, C. An empirical study into laser sintering of ultra-high molecular weight polyethylene (UHMWPE). *J. Mater. Process. Technol.* **2010**, *210*, 72–80. [CrossRef]
29. Gibson, I.; Shi, D. Material properties and fabrication parameters in selective laser sintering process. *Rapid Prototyp. J.* **1997**, *3*, 129–136. [CrossRef]
30. Jones, B.; Nachtsheim, C. Split-Plot Designs: What, Why, and How. *J. Qual. Technol.* **2009**, *41*, 340–361. [CrossRef]
31. Siebertz, K.; van Bebber, D.; Hochkirchen, T. *Statistische Versuchsplanung: Design of Experiments (DoE)*, 2nd ed.; Springer: Berlin/Heidelberg, Germany, 2017. [CrossRef]
32. Tabelle der Varianzanalyse für Faktoriellen Versuchsplan Analysieren. Available online: https://support.minitab.com/de-de/minitab/20/help-and-how-to/statistical-modeling/doe/how-to/factorial/analyze-factorial-design/interpret-the-results/all-statistics-and-graphs/analysis-of-variance-table/ (accessed on 26 March 2023).
33. Stahel, W. Purposes and strategies in regression analysis. *J. Stat. Plan. Inference* **2004**, *122*, 175–186. [CrossRef]

34. Übersicht über Zentral Zusammengesetzte Versuchspläne. Available online: https://support.minitab.com/de-de/minitab/21/help-and-how-to/statistical-modeling/doe/supporting-topics/response-surface-designs/summary-of-central-composite-designs/ (accessed on 26 March 2023).
35. Baumann, F. Additive Fertigung von Endlosfaserverstärkten Kunststoffen mit dem ARBURG Kunststoff-Freiform Verfahren. Ph.D. Thesis, Karlsruher Institut für Technologie, Karlsruhe, Germany, 2020.
36. Hoesch, F. Development of an Experimental Setup for Twisting Carbon Fiber for Additive Fabrication of Fiber Reinforced Plastics. Bachelor's Thesis, Karlsruhe Institute of Technology, Karlsruhe, Germany, 11 April 2022.